Wear 592 (2026) 206593

Contents lists available at ScienceDirect

Wear

journal homepage: www.elsevier.com/locate/wear

Modeling brake emissions using an *ad hoc* physics-inspired recurrent neural network

Stefano Candeo [a,*], Ana Paula Nogueira [b], Giovanni Straffelini [a], Mauro Da Lio [a]

[a] Department of Industrial Engineering, University of Trento, Via Sommarive 9, Povo, Trento, Italy
[b] Brembo N.V., Stezzano, Via Stezzano 87, 24126, Bergamo, Italy

ARTICLE INFO

Keywords:
Brake
Emissions
Modeling
Neural network

ABSTRACT

Brake emissions have gained increasing attention over the past twenty years. Still, due to the inherently transient and complex nature of brake emissions, advanced modeling techniques are necessary but remain limited in the existing literature. In this study, randomized tests were conducted on a reduced-scale dynamometer with braking parameters within the domain of the Worldwide Harmonized Light Vehicles Test Procedure (WLTP). Emissions were measured using an Optical Particle Sizer (0.3-10 μm) and modeled with a Neural Network (RNN) featuring an *ad hoc* recurrent architecture. The RNN model comprises: 1) an Internal State, s, which describes the bedding-in process and surface-state transitions caused by changes in braking parameters, and 2) a stationary component, e_0, which depends solely on dissipated energy and brake deceleration. WLTP data were used to test the model. Additional randomized tests were then conducted, yielding strong R^2 values ranging from 0.96 to 0.99 for cumulative emissions and lower values of 0.55 to 0.60 for individual events.

1. Introduction

In recent decades, non-exhaust emissions have garnered increasing attention, as their relative contribution to air quality has become significant. Non-exhaust and wear-related emissions from brake materials, tires, road surfaces, and their resuspension contribute significantly to ambient PM10 and environmental release [1]. Regarding brake wear, studies have shown that in urban environments, it can contribute up to 55% of non-exhaust PM10 emissions by mass [2], and up to 21% of total traffic-related PM10 emissions [3–5]. Approximately 40–50% of brake wear is estimated to become airborne particles, with 80–98% falling within the PM10 range and 56–70% within the PM2.5 range [6].

While pioneering studies on brake wear particles were conducted in the early 2000s [7,8], the first regulatory measure targeting non-exhaust emissions is expected to come into force in 2026 with the implementation of EURO 7, which introduces PM10 emission limits for light-duty vehicles. Recent and ongoing research has primarily focused on the influence of materials [9–13], particulate matter characterization [14–18], and testing aspects [10,19–23]. Brake emissions are characterized by a combination of transient and history-dependent phenomena, including bedding-in processes [10,14,24–27], surface-state transitions induced by changes in braking parameters, and complex interactions between operating conditions and tribological interfaces [11,19,28–30]. These effects lead to non-stationary emission behavior that is hardly captured by steady-state or purely energy-based models alone.

Straightforward mitigation strategies are closely linked to emission sources. Regarding the brake material impact, Non-Asbestos Organic (NAO) brake pads already display low-emission characteristics [9,11,12,16,22,23,31]. In contrast, low-metallic pads likely require modifications to their composition or coupling with counter face discs that provide improved wear resistance compared to conventional cast iron discs through chemical modifications, surface treatments [32], or the deposition of hard metal coatings [12,13,26,33].

The selection of brake couples with low-emission characteristics is crucial because it directly reduces emissions at the source. In addition to material solutions, other mitigation strategies focus on hardware or system design. For instance, the adoption of drum brake systems is likely to reduce emissions, as their enclosed design is inherently more effective at limiting the release of particulate matter compared to disc brake systems [13,34]. Alternatively, brake particle collection filters are being developed to directly capture emitted particles, using either grooved brake pad designs [35,36] or enclosed configurations surrounding the disc [37–39].

* Corresponding author.
E-mail address: stefano.candeo@unitn.it (S. Candeo).

https://doi.org/10.1016/j.wear.2026.206593
Received 12 September 2025; Received in revised form 14 January 2026; Accepted 11 February 2026
Available online 19 February 2026

Besides these strategies, software-based approaches that utilize prior knowledge of the relationship between driving style and emission levels can lower emissions through optimized decelerations. However, evaluating their effectiveness and integrating them into vehicle systems is complex, especially due to safety regulations and system architecture limitations. Although these solutions have not yet been widely implemented in industry, they hold significant promise, particularly within the context of software-defined vehicles (SDV) and Cooperative, Connected, and Automated Mobility (CCAM).

Related to the latter mitigation strategy, software-based brake systems require emission models to optimize brake strategies. In the authors' opinion, although the literature is extensive in experimental studies, predictive models are limited, and current knowledge is insufficient to support the development of software-based solutions.

Understanding the influence of the braking parameters is key to modeling emission behaviors, and although several efforts have been made, there still exist open questions and contradictory results. For instance, the influence of brake deceleration or pressure was found to increase PN10 [28,40] while other studies reported no significant or lower impact [11,30].

A physical correlation is generally expected between dissipated energy and particulate matter emissions [22,41,42]. Kinetic energy scales with the square of the velocity and with vehicle mass. With respect to vehicle mass, or load, a few studies [22,30,43] evaluated identical friction materials under different load conditions and observed a linear positive correlation between load and particulate emissions. Whereas other studies [43,44] have identified slightly sub-linear relationships between vehicle mass and PM emissions, suggesting that heavier vehicles do not increase emissions proportionally. As a final remark on the influence of vehicle load, the review study [9] conducted a database analysis and reported a weak correlation between vehicle load and PM10 levels, which may be attributed to the significant variability in friction material compositions.

Linear relationships between dissipated energy and emissions have also been reported in the studies by Park et al. [45] and Men et al. [41]. However, the influence of velocity on emissions is not simple. In this regard, Nieman et al. [28] and our previous work [11] identified cubic relationships, indicating that velocity may contribute to PM emissions in a nonlinear manner. These power-law trends are broadly consistent with experimental observations [40,42]. Overall, the complexity of the brake emission phenomenon is influenced not only by energy and velocity, but also by factors such as material history [19] and surface conditions [46].

Regarding the influence of temperature (T) on brake emissions, the transition temperature for ultrafine particle formation is a critical characteristic. It typically occurs above 170-200 °C [47,48], beyond which PN emissions may escalate by orders of magnitude. The studies [19,41] have reported positive correlations between temperature and both PM10 and PN10 emissions, noting strong sensitivity that depends on the specific friction materials and material history [19]. Conversely, on-road driving measurements have shown no significant effect of temperature on PM10 emissions, and a recent study [49] found that including the pad temperature did not significantly improve the accuracy of the wear model.

In the context of emission modeling, Niemann et al. [28] developed an advanced brake cycle based on drag-operated braking events to investigate the influence of history effects and braking parameters on the emission behavior. These aspects are particularly noteworthy, as braking conditions such as velocity, contact pressure and temperature govern the surface characteristics, which in turn influence brake performance and emission behavior. Notably, as part of this investigation, the authors developed a black-box model that predicts particulate emissions during the WLTP cycle with an accuracy of 80%.

Men et al. proposed a parametrization of PM emission based on energy dissipation and other tribological considerations [41]. Power-law relationships based on initial velocity [41,42] and dissipated energy [12] were used to enhance model accuracy and to enable meaningful comparisons between the WLTP and other driving cycles, respectively.

Considering the nonlinear and complex relationship between braking parameters and emissions, as well as the transitional nature of emissions, Machine Learning (ML) and Deep Learning (DL) approaches have strong potential. However, only a few have specifically applied them to brake emissions. Wei et al. [50] applied various ML algorithms to a dataset of approximately 200 braking events under urban driving conditions. At the same time, Ye Liu et al. [44] employed a gradient boosting technique on WLTP data to evaluate the effect of braking parameters. Additionally, it is worth noting that Ye Liu et al. [51] developed an emission model based on pin-on-disc experiments conducted under varying pressure (P) and velocity (V) conditions. The resulting PV maps were then integrated into a Finite Element Analysis (FEA) framework to predict PM emissions from a WLTP brake cycle with a relative error of 9–12%

Regarding the application of deep learning techniques, Ricciardi et al. [52] employed an Artificial Neural Network (ANN) on vehicle data. Our previous study [53] utilized an ANN on dynamometer data, which was then fed into a simulator to predict emissions at road intersections based on vehicle dynamics. While advances in brake emission modeling remain limited overall, recent contributions point toward a growing use of data-driven methodologies to address the complexity of brake emission behavior.

1.1. Contribution

To capture the transient nature of the phenomenon, this paper employs a Recurrent Neural Network (RNN) trained on experimental emission data within the fine–coarse particle fraction range of 0.3–10 μm. We break down emissions into two components: a stationary component, which is modeled as a function of brake deceleration and dissipated energy, and a dynamic component, which uses a state variable to capture non-stationary dynamics through a multiplicative emission factor. This state captures both long-term (i.e., bedding) and short-term emission fluctuations resulting from the sequence of braking events. The training examples were generated by randomly selecting braking parameters from the WLTP domain and were evenly distributed within it. The model is explicitly designed with two inputs: dissipated energy and brake deceleration. However, since it's a dynamical model, the sequence of inputs also plays a role, which is captured by the varying state variable. We evaluated the model's accuracy for both individual brake events and cumulative emissions. Finally, we discuss the model's implications and challenges for brake emission modeling and its applications in real-world settings.

2. Experimental procedures

2.1. Brake materials and dynamometer

In this study, a commercial resin-based low-metallic Cu-free brake friction material was used for the tribological tests. The samples have a rectangular geometry (12 mm × 30 mm) and were cut from a commercial pad (Fig. 1). The disc sample is made of pearlitic cast iron with a hardness of 235 HV10. The samples have a diameter of 120 mm, a thickness of 6 mm, and an effective test radius of 50 mm.

The tribological tests were carried out with the reduced-scale dynamometer LINK model 1200, shown in Fig. 2a. A view of the chamber with the pad and disc in contact is depicted in Fig. 2b. To ensure the same specific brake energy and similar local conditions of sliding velocity and contact pressure as those of a reference vehicle, in this case a D-segment, a mechanical similitude is used to determine the actual brake parameters, such as shaft rotational speed, inertia, and applied pressure. More details on the scaling relationships and material compositions can be found in the previous study [11,54]. The temperature of the disc was monitored with a K-type thermocouple.

Fig. 1. Friction materials and brake disc samples.

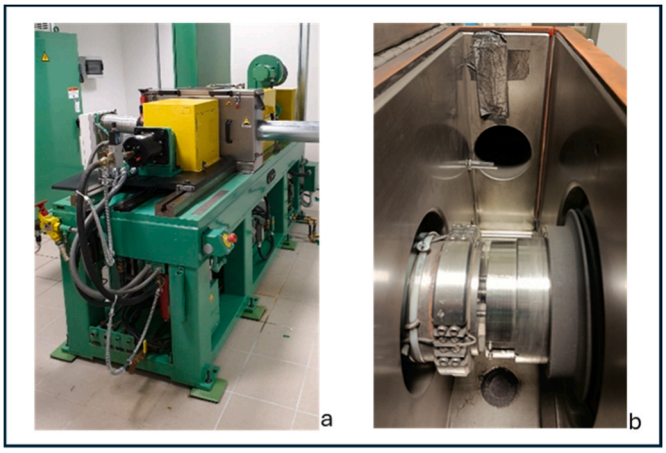

Fig. 2. LINK M1200 reduced-scale dynamometer (a) and internal view of the chamber with pad and disc in contact (b).

2.2. Brake cycles

To create the training and test data, we employed two brake cycles: WLTP and Randomized brake cycles.

2.2.1. WLTP cycle

Through statistical analysis of an in-use driving database, the Worldwide Harmonized Light Vehicles Test Procedure was developed to closely represent real-world driving conditions [55]. The related data consists of 303 brake events. The average speed is 43.7 km/h, and the maximum initial vehicle speed is 132.5 km/h, while the brake deceleration ranges from 0.49 m/s^2 to 2.18 m/s^2, with a mean value of 0.97 m/s^2. Detailed brake parameters are presented in Fig. 3 as cumulative distribution functions of initial, final velocities, speed variation, and brake deceleration.

In the WLTP brake cycle, the procedure for the surface preconditioning, or *bedding*, involves repeating the brake cycle five times to stabilize friction and emissions before the actual test.

In this cycle, the brake stops are predefined, both in the order of the events and in the parameters of each event, which limits the ability of any data-driven method to learn and generalize to a broader range of events and ordering.

2.2.2. Randomized brake cycles

To avoid deterministic patterns in the sequence of braking events and to uniformly sample the WLTP parameter space, randomized brake cycles were introduced. While the standard WLTP preserves representative driving patterns, randomization enables improved generalization by decorrelating successive events. History effects neglected by randomization are explicitly captured by the internal state variable, s, which represents the evolving surface condition and retains memory of prior braking events.

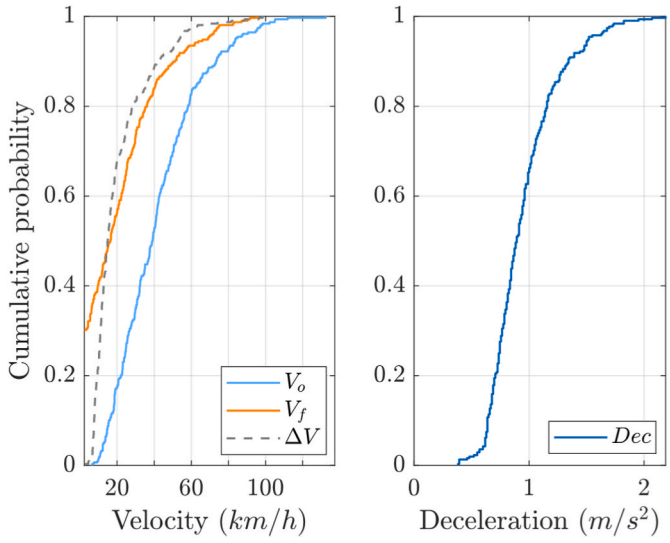

Fig. 3. Cumulative distribution function of the initial, final velocities and speed variation (left), and brake deceleration (right) in the WLTP brake cycle.

Because the final velocity cannot be negative, the set of mean velocity–speed variations forms a trapezoidal domain, as shown in Fig. 4, with data points evenly distributed throughout the area. The speed variation ranges from 10 to 65 km/h, while the mean speed varies from 10 to 125 km/h. Then, to build the brake cycle, the initial and final vehicle speeds are calculated and combined with uniform distribution values for the brake deceleration in the range of 0.4-2.2 m/s^2, which is similar, as mentioned, to that of the WLTP cycle.

Table 1 gives an example of the braking parameters and the measured output for a randomized test.

2.2.3. Datasets

We used two randomized brake cycles and three WLTP cycles, as shown in Table 2. Dataset 1 was used for training, while the remaining datasets were used for testing the model. Dataset 3 consists of four repetitions of the WLTP cycle, while Dataset 4 is the fifth repetition. Dataset 5 includes seven repetitions of the modified WLTP. Fresh samples were used in datasets 1, 2, 3, and 5.

In both WLTP and Randomized tests, braking is applied in deceleration mode. The fixed sequence of brake stops and the intensity of each

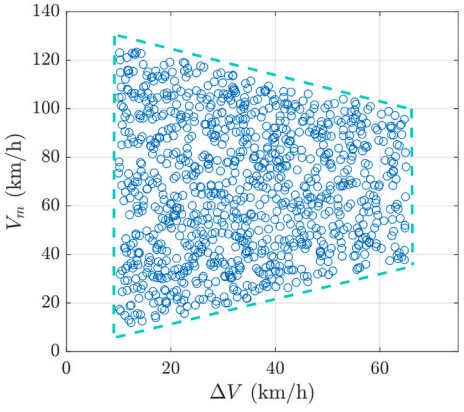

Fig. 4. Mean vehicle speed versus speed variation in the randomized brake cycle.

Table 1
Example of the braking parameters and outputs for the Randomized test A.

v_0 (km/h)	v_f (km/h)	d (m/s^2)	T_0 (°C)	T_{max} (°C)	Duration (s)
67.5	21.3	0.60	113.2	130.8	21.61
105.9	43.3	2.14	106.6	179.1	8.282
46.9	23.4	1.15	126.3	137.4	5.807
87	67.8	1.24	113.1	141.3	4.42
67.2	49.5	2.25	109.5	132.3	2.308
119.3	87.8	1.26	103.1	168.8	7.021

Table 2
Datasets of the study.

Dataset	1	2	3	4	5
	Randomized A (training set)	*Randomized B*	*WLTP 1-4 (four WLTP cycles)*	*WLTP 5 (after bedding with the four WLTP cycles)*	*Mod. WLTP 1-7 (seven WLTP cycles)*
Brake stops	*2772*	*1963*	*1212*	*303*	*2121*

stop in the WLTP cycle determine the disc temperature evolution during the test, which generally stays below 140-170 °C with peaks below 170 °C [55].

During the randomized brake test of the WLTP, brake stops were set at intervals of 50-60 s to prevent overlap in the emission signals and to limit the brake disc temperature. This interval strikes a balance between avoiding excessive overheating of the brake discs, which can occur due to frequent high-intensity braking, and keeping the test duration reasonable. As described in Section 3.3, this time interval allows the emission signal to return to baseline before the subsequent brake stop is applied, ensuring that emissions from different brake stops do not overlap and each brake stop is associated with its emission value. In addition, to avoid emission signal overlaps in the WLTP cycle (see section 2.3), in one dataset (Mod. WLTP 1-7), the WLTP cycle was modified to extend the brake cycle to a minimum interval of 40 s.

Fig. 5 compares the cumulative distributions of the disc temperature for the tests: Randomized (A and B), the WLTP, and the Modified WLTP. During the WLTP braking events, the average disc temperature was 69.6 °C, with a peak temperature reaching 162 °C. In comparison, the Modified WLTP yielded slightly lower disc temperatures, with an average of 62.5 °C and a maximum of 159.7 °C. The increased cycle time

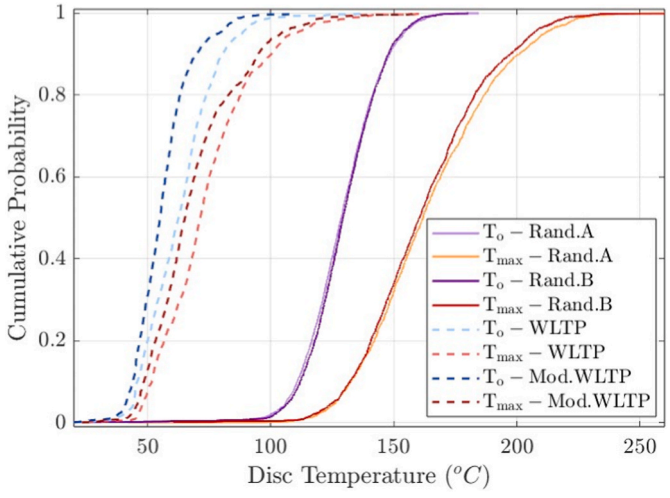

Fig. 5. Cumulative distribution functions of the disc temperature for the Randomized tests and WLTP.

for the selected brake stops allowed for longer cooling intervals between braking events, resulting in reduced thermal buildup and overall lower disc temperatures. In contrast, the randomized test resulted in significantly higher disc temperatures, with an average ranging between 148 and 150 °C and with approximately 10% of the maximum disc temperatures falling between 200 °C and 248 °C.

2.3. Emission measurement

Fig. 6 shows a schematic representation of the experimental setup for emission measurements, comprising the fan, HEPA filter, test chamber, sampling lines, and the Optical Particle Sizer (OPS). Airborne particles were measured using a TSI® OPS, which detects concentrations of concentrations up to 3000 particles/cm^3 within the 0.3–10 μm size range. The measurements are recorded across 16 size channels at a frequency of 1 Hz. The sampling point was placed 1 m from the chamber outlet, and isokinetic conditions were maintained during measurements. A diluter was connected upstream of the OPS to introduce a dilution factor of 10 in the airflow. The emission values are expressed to account for the applied dilution factor. The inlet airflow velocity was approximately 1.1 m/s, corresponding to an airflow of about 0.8 m^3/min and an air exchange rate of 20 times per minute. Additional details of the set-up can be found in the previous study [25].

The evolution of emitted particles was determined by synchronizing the OPS data with the data acquisition system of the dynamometer. The cumulative particle numbers for each size bin were obtained by summing the particle counts until the signal returned to the baseline. As shown in Section 2.4.2, we develop a model that predicts emission volumes. Therefore, the particle counts were converted to spherical-equivalent volumes for each bin (a particle of diameter d was counted as a nominal volume). The total emitted volume is calculated as the sum of the volumes across all size bins.

While particle emissions are usually reported as numbers or mass, several studies have presented them in terms of volume, also calculating equivalent particle densities using gravimetric methods [19] or other techniques [56]. From a modeling perspective, using volume as the output variable is beneficial because it is less affected by variations in particle diameter (see Section 2.4.2). Consequently, modeling the total particle volume with a single output is computationally simpler than creating separate models for each size bin and summing their results.

For the randomized tests, the time between brake events was approximately 50–60 s. As this interval was sufficient to allow the signal to return to baseline between stops, it was possible to obtain a representative cumulative emission value for each brake event. On the other hand, in the standard version of the WLTP cycle, several time intervals between brake stops are too short to associate each stop with a representative cumulative emission value, as the emission signals from different braking events may overlap. Fig. 7 illustrates the emission signal associated with specific brake stops in the standard WLTP brake cycle. The cross symbols denote the instant at which the brake event begins. The following emission peaks are delayed by 3.5 s. The emission signal from a single event takes approximately 20 s to reach the baseline. The decay time depends on several factors, such as the settling time of particles, the velocity of airflow, the system volume, and the braking intensity.

To address signal overlap, cumulative emission values for this test were calculated by summing emissions from the start of one brake stop to the start of the next. Although this approach makes each value less representative of an individual brake event, it ensures consistency across all stops. Emissions are not double-counted, as those assigned to one brake stop are excluded from the next. As will be shown in Section 3.3, the R^2 values remain robust when applying a moving average over three consecutive brake stops. Finally, the Modified WLTP dataset, with a minimum cycle time of 40 s, was tested to evaluate the accuracy of the model without overlap in the emission signal, and the resulting R^2 values were consistent with those obtained from the other datasets (see

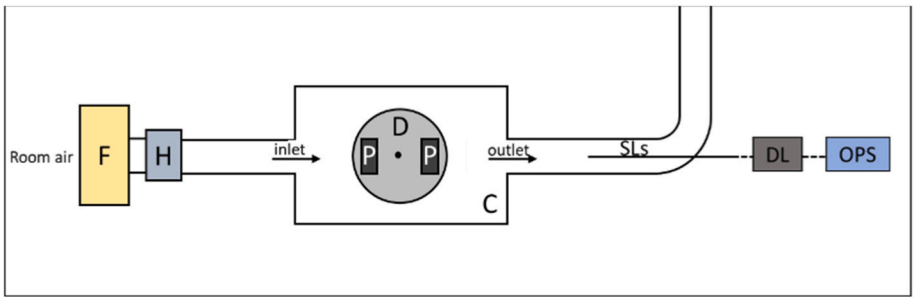

Fig. 6. Scheme of the experimental setup: the fan (F), HEPA filter (H), chamber (C), disc (D), pad (P), sampling lines (SLs) and the OPS.

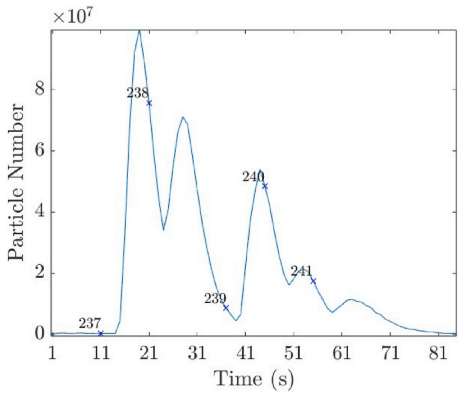

Fig. 7. Total particle number for specific brake stops of the standard version of the WLTP brake cycle. The numbered markers indicate when individual brake events begin.

Section 3).

2.4. Neural network model

We aim to develop an efficient and interpretable neural model that maximizes prediction accuracy while minimizing the number of parameters. Although general-purpose neural architectures can also fit the data, they often lack explainability and usually require more parameters than ours. This increase in parameters raises the risk of overfitting and diminishes the model's ability to generalize (e.g., see Ref. [57]). Instead, we can create an efficient and interpretable model by integrating domain knowledge into the neural structure.

2.4.1. Choice of the input parameters

To design the neural architecture, we begin by identifying the parameters that influence emissions based on expert knowledge and ranking them by importance. These parameters are selected from those used in the experiment.

- The initial velocity v_0.
- The final velocity v_f.
- The deceleration d, which combined with the two above determines the event duration τ.
- The initial temperature T_0.
- The average temperature T_{avg} and the maximum temperature T_{max}.

Domain knowledge indicates that emissions (e) are mainly influenced by dissipated energy, which is proportional to the difference in the squares of the initial and final velocities ($v_0^2 - v_f^2$), and by contact pressure, which impacts the severity of wear. The contact pressure determines the brake force, which then causes the observable deceleration (d). For instance, a model that learns the function $e = f\left(v_0^2 - v_f^2, d\right)$, or more concisely:

$$e = f\left(\Delta v^2, d\right) \tag{1}$$

This model does not consider the average velocity, $v_{avg} = 0.5\left(v_0 + v_f\right)$, and the initial temperature (T_0). Conversely, maximum and average temperatures are strongly correlated with dissipated energy and do not need to be accounted for separately. In fact, Δv^2 implicitly accounts for any increase in temperature. By constructing the model so that $e = f(\Delta v^2, d)$, the excluded parameters, v_{avg} and T_0, act as unmodeled noise. We will later be able to assess their relative importance alongside other noise sources by evaluating the model's prediction residuals.

2.4.2. Choice of the output quantity

We need to clarify what the model predicts, specifically, the quantity referred to as e. As illustrated in Fig. 8, the number of particles in each diameter range is inversely proportional to the cube of the diameter. Therefore, we have chosen to predict the "nominal" emission volumes (as if the particles were on average spherical), which stay roughly the same across different diameter bins. This method allows us to weigh all bins equally. In contrast, if we predicted the number of particles, larger particles would have less influence on the model, leading to a focus on predicting the smallest bins.

2.4.3. Modeling the process dynamics (bedding)

The model given in (1) represents a static process. However, for the same input $\{\Delta v^2, d\}$, real emissions are greater with fresh pads and tend to progressively decrease with the following brake events, a phenomenon known as bedding. Given the same input, (1) would, however, predict the same output regardless of the history of the previous events. It can capture the average emissions, but it cannot describe the dynamics of bedding.

To capture bedding, we need a discrete-time dynamic model, i.e., a

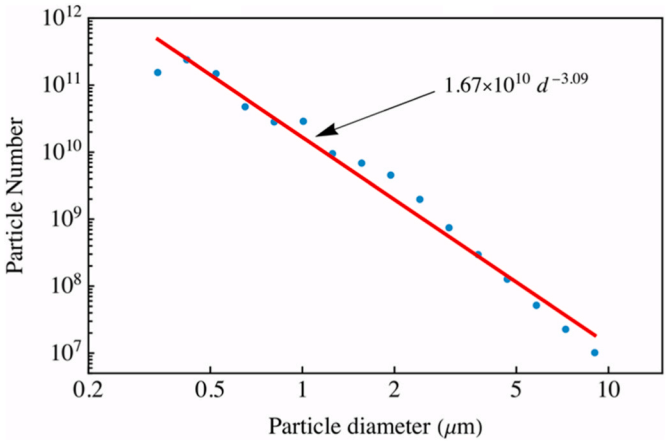

Fig. 8. Cumulative Particle Number as a function of particle diameter in the test Randomized A.

model in which the output $\boldsymbol{y}_k$ (emissions) at the discrete time k (the k-th brake event) is a function of the input $\boldsymbol{u}_k$ (brake parameters) and of the system state $\boldsymbol{s}_k$ (state of the pad) at that time, such as, e.g., $\boldsymbol{y}_k = \boldsymbol{F}(\boldsymbol{s}_k, \boldsymbol{u}_k)$. The changes in the system state are modeled with another equation, such as, e.g., $\boldsymbol{s}_{k+1} = \boldsymbol{G}(\boldsymbol{s}_k, \boldsymbol{u}_k)$, which describes the new state following $\boldsymbol{s}_k$, $\boldsymbol{u}_k$.

Hence, we update model (1) as follows:

$$e_k = \mathrm{s}_k f\left(\Delta v_k^2, d_k\right) \tag{2}$$

This means that the emissions at event k, (e_k), are a function of the surface state (s_k) and of the input $\left(\Delta v_k^2, d_k\right)$ at time k. In (2), we model the state space $\boldsymbol{s}_k$ with a one-dimensional (scalar) quantity s_k. Furthermore, (2) gives a structure to the generic function $\boldsymbol{F}(\boldsymbol{s}_k, \boldsymbol{u}_k)$, which now reads $\mathrm{s}_k f\left(\Delta v_k^2, d_k\right)$. This modeling choice reduces the class of functions that can be approximated, but makes the state s_k interpretable, because it represents the *amplification factor* for the emissions $f\left(\Delta v_k^2, d_k\right)$. During the bedding process, s_k will be higher with fresh pads and will gradually decrease with subsequent brake events. For the state update, we also give a structure to $\boldsymbol{G}(\boldsymbol{s}_k, \boldsymbol{u}_k)$ as follows:

$$s_{k+1} = g(\mathrm{s}_k, e_k) \tag{3}$$

Where the effect of the input $\Delta v_k^2, d_k$ is lumped into the emissions e_k they caused, i.e., we assume that the variation in the surface state depends on the previous emission, rather than on $\Delta v_k^2, d_k$ separately. This assumption is a modeling choice that is indirectly supported by the quality of the model predictions. Still, its generalization to other material pairs or more severe braking regimes is not implied. We further structure the model as follows:

$$s_{k+1} = g(\mathrm{s}_k, e_k) = s_k - \Delta s_k \tag{4}$$

Where the variation Δs_k in the system state is modeled as follows:

$$\Delta s_k = e_k \, h(\mathrm{s}_k, e_k) \tag{5}$$

Equation (5) imposes that the variation in the system state is zero if the emissions are zero. Equations (4) and (5) form the recurrent part of the model, which, given the initial state (s_1), and a sequence of emissions (e_k), predict the future states (s_{k+1}). In (2,5), the functions $f()$ and $h()$ are neural networks that will learn the sub-models for baseline emissions (2) and for the state dynamics (4,5).

A block diagram for the neural implementation is shown in Fig. 9. On top, the input is a sequence of brake events ($v_{0\,k}, v_{f\,k}, d_k$). A first module (a) computes (what would be) the baseline, or stationary, emissions $\widehat{e}_k = f\left(\Delta v_k^2, d_k\right)$ and a second module (b) computes the actual emissions according to (2), i.e., $e_k = \mathrm{s}_k \, \widehat{e}_k$, and updates the system state according to (4,5). We present here the final architecture, obtained after several variations in the number of neurons, layers, and topology (e.g., see Appendix in Ref. [58] for an example of hyperparameter choice).

The block (a) that learns $f\left(\Delta v_k^2, d_k\right)$ is shown below on the left. A first algebraic layer combines v_{0k} and v_{f_k} into Δv_k^2, which, together with d_k, enters a neural layer with 20 neurons, followed by Tanh activation and a neural layer with a single neuron. At this point, the network may produce a scalar output, which can be either positive or negative. Since emissions can only be positive, we append a "*softplus*" operator, $Log(Exp(x) + 1)$, that re-maps the input domain to the real positive axis, i.e., $]-\infty, \infty[\rightarrow]0, \infty[$. A final neuron, with no biases, rescales the output. The number of parameters in this sub-network is 82.

The block (b), at the right, implements the recurrent part, shown in detail in (c) and (d). In particular (c) shows the computation of (2) in the form of a product between s_k and the baseline emissions $\widehat{e}_k$ from block (a). Finally, block (d) shows the implementation of (4,5). The upper branch computes Δs_k using a neural network with structure 5-Tanh-1 that learns the function $h(\mathrm{s}_k, e_k)$. The rest are algebraic operations to realize (4,5). The number of parameters in this branch is 21. The total number of parameters for the model is 104, counting the two branches and the initial state s_1.

2.5. Training

The network is trained using dataset 1 as the training set. Datasets 2-5 are saved for test sets. Given that the training set comprises 2773 examples and the network parameters are 104 (i.e., the number of examples is 27 times the number of parameters), we preferred not to use a validation set in the training process, reserving dataset 2 for testing.[1] We trained on dataset 1 for 50,000 epochs, which is a single history of 2773 steps. Since the model is a dynamical system with a one-dimensional internal state, the first 50 braking events were discarded to reduce the possible impact of strong initial transients related to the early bedding-in phase, which may require a higher-dimensional state space to be fully captured; sensitivity tests with different numbers of discarded events showed stable dynamics, and 50 events were conservatively selected.

The input-output data were normalized as follows. The velocity was normalized by 120 km/h, in such a way that 95% of the input example velocity spanned the interval 0-1. The deceleration was divided by 2.5 $\mathrm{m/s^2}$, in such a way that 95% of the input signal also spanned the interval 0-1. The output was finally normalized using the same logic by dividing the measured volumes by 10^8 cubic μ m, in such a way that the output represents tenths of cubic mm.

The training Algorithm was the ADAM optimizer. All computations were carried out in Wolfram's Mathematica (versions 12.3.1 and 14.2.1).

2.5.1. Loss function

The optimization process used two loss functions. The mean squared loss was used for the network predictions e_k. In addition, we used a mean squared loss layer weighted by a factor 0.09 on baseline predictions $\widehat{e}_k$:

$$mean\left[(e_k - \overline{e}_k)^2\right] + 0.09\, mean\left[(\widehat{e}_k - \overline{e}_k)^2\right] \tag{6}$$

In this way, while the model seeks to minimize the square error of predictions, it also tries to keep $\widehat{e}_k$ close to the mean emissions.

2.6. Estimating the initial state

So far, the model 2.4.3 Modeling the process dynamics (bedding) consists of two learned functions $h(\mathrm{s}_k, e_k)$ and $f\left(\Delta v_k^2, d_k\right)$, and is implemented with two neural networks (Fig. 9a and d, respectively). Given a sequence of brake events ($v_{0\,k}, v_{f\,k}, d_k$), the model predicts emissions and the evolution of the pad state s_k, given the initial pad state s_1 (Fig. 9 b).

During the model training (section 2.5), the initial state of the training dataset (Dataset 1) is automatically estimated. However, this state may not be valid for the other datasets because it is unlikely that the initial surface state is the same. This is particularly true for dataset 4, which refer to conditions following a previous bedding process.

To estimate the initial state for the test datasets (datasets 2-5) the model was trained for a few epochs on each dataset separately. The first 50 braking events are discarded to limit the influence of short-term transients that the proposed model, which employs a one-dimensional internal state, cannot fully capture. However, the initial state may still differ across datasets due to varying initial surface conditions; for this reason, it is estimated explicitly for each test dataset while keeping the network parameters fixed. For example, the initial state of WLTP5 is

[1] When training neural models, there are usually three types of data: the *training set* is the set of examples that the optimization algorithm uses for gradient descent, the *validation set* is the set of independent examples used by the algorithm to monitor overfitting and eventually stop learning (as such the validation set intervenes in selecting the final model). Finally, the *test set* is another independent dataset which did not appear in either training or selection of the model.

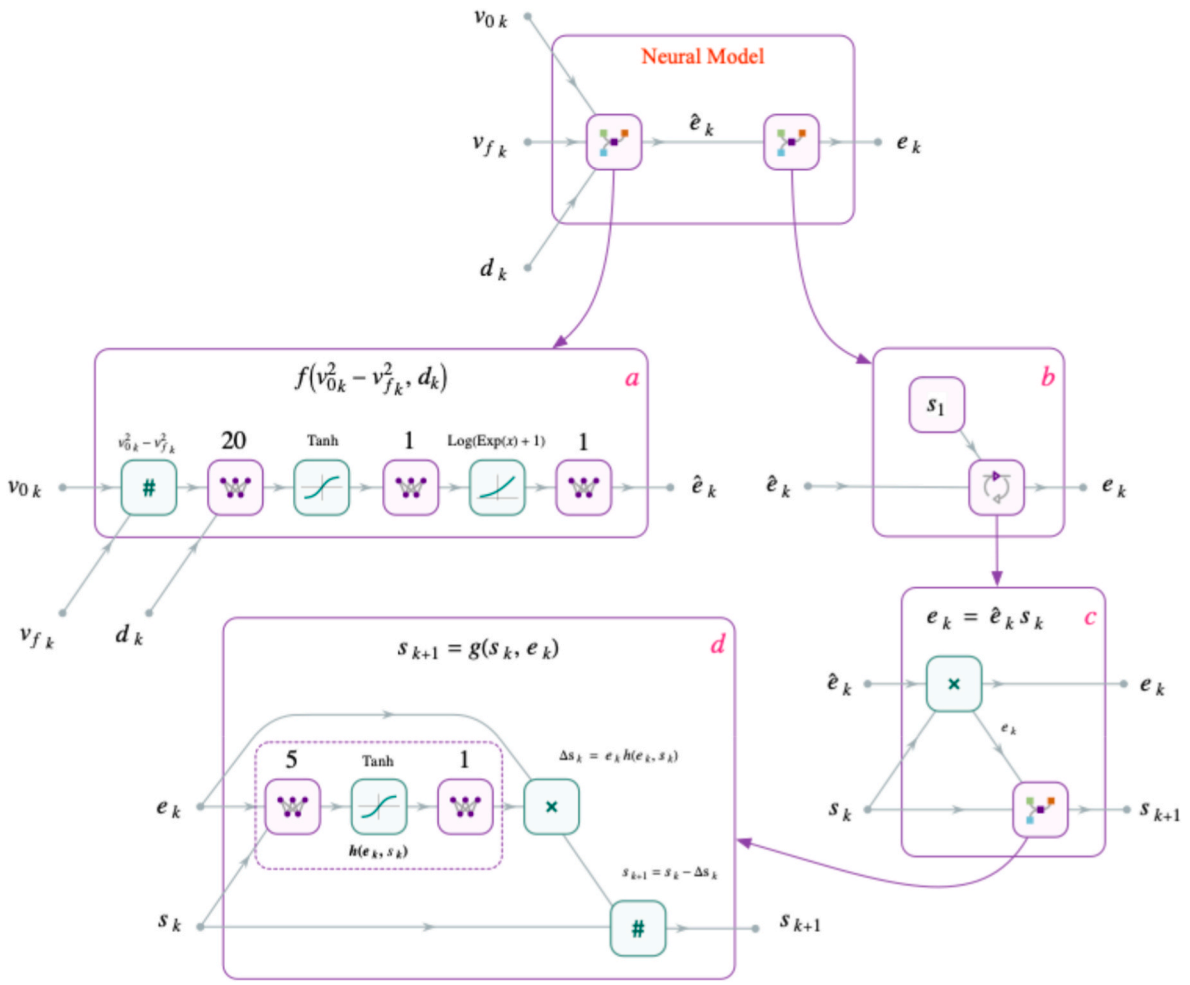

Fig. 9. Block diagram of the recurrent neural network model, composed of one module (a) that learns the function in (2) and a second module (b) that learns the state dynamics (3). Both modules have physics-informed structures.

identified as the final state reached after the WLTP1–4 sequence, consistently reflecting a post-bedding surface condition.

The parameters of $h(s_k, e_k)$ and $f(\Delta v_k^2, d_k)$ were frozen, to preserve the baseline emissions and the model dynamics. Only s_1 was allowed to change. The estimated initial states are shown in Table 3. Notably, datasets 1 and 2 have an almost identical initial condition (they were very similar), whereas the initial state of dataset 4 is close to unity because they refer to a post-bedding state.

3. Results

3.1. Internal state

Fig. 10 illustrates the evolution of the internal state, as described in (4-5), starting from the initial state estimated in Section 2.6.[2] The state, which is the amplification of row emissions according to (2), gradually decreases. This means that, with repeated brakes, emissions decrease toward a (pseudo) asymptotic limit.

However, the decrease is not monotonic. Sometimes the state steps back to higher values. This is particularly evident in the case of a hard brake before the end of the WLTP cycle, as shown in the inset (section 4 will further discuss this case). Smaller state steps back are also visible in the two randomized datasets 1 and 2.

To investigate the conditions that cause an increase in the surface state, we study the state variation as in (5), i.e. $\Delta s_k(s_k, e_k) = e_k\, h(s_k, e_k)$. We extract the subnetwork that computes Δs_k from the trained network (Fig. 9d) and show the contour plot of $\Delta s_k(s_k, e_k)$ in Fig. 11. The green area indicates the conditions (s_k, e_k) that result in a decrease in the state. Conversely, the red area corresponds to increasing states. The red dashed rectangle visualizes the domain of the training data (hence, outside that rectangle, the network is extrapolating).

As the chart shows, for a given state s_k, a decrease is obtained if the emissions are below a certain threshold (the boundary between green and red). For larger emissions, the state steps back. In other words, light braking in the green area enhances the bedding, while harsh braking in the red area deteriorates it.

Furthermore, the smaller the state, the lower the threshold, meaning that lighter braking may be sufficient to step back slightly. This also implies that the bedding process does not tend to a stable asymptotic limit because it can be reversed with energetic brakes.

Table 3
Initial surface states.

Dataset	1	2	3	4	5
Estimated s_1	*1.98*	*1.94*	*2.79*	*1.35*	*1.32*

[2] Because of the loss function (6), the average state is close to unity for dataset 1.

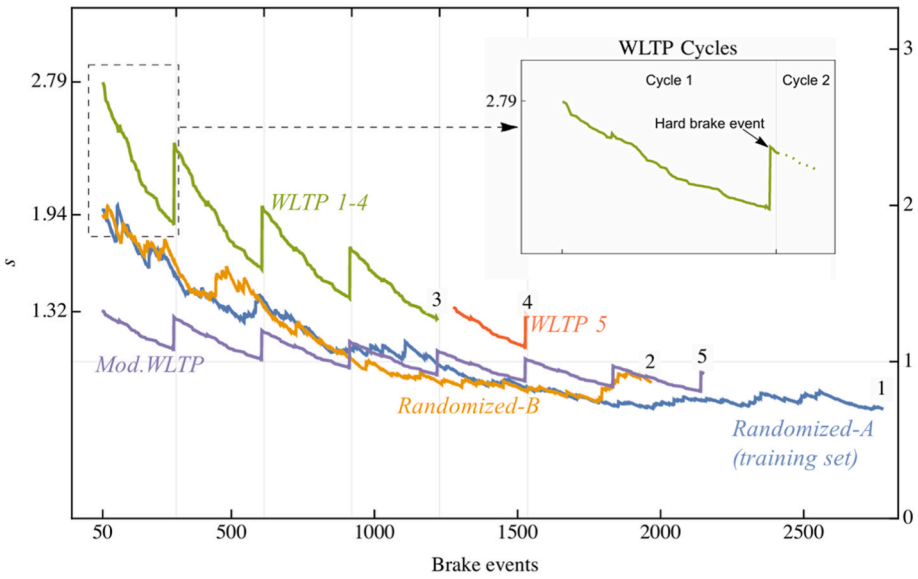

Fig. 10. Evolution of the Internal State for the five datasets.

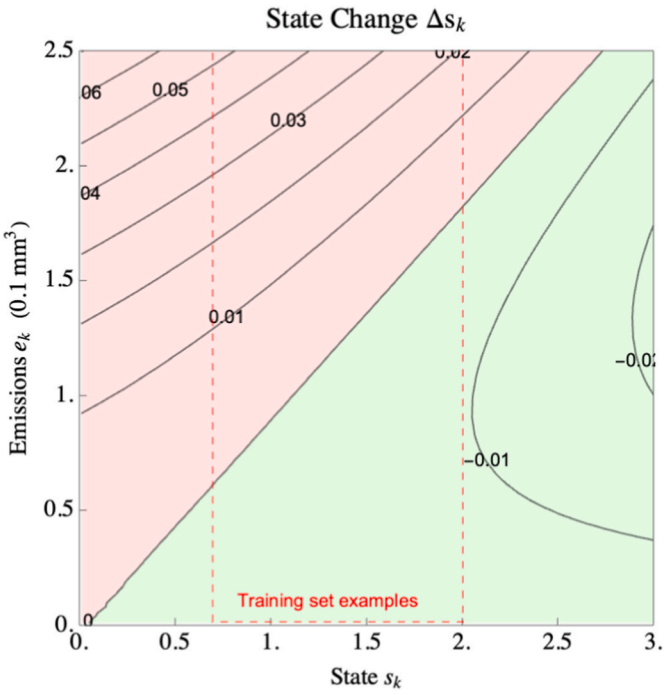

Fig. 11. Contour plot of the state variation Δs_k as a function of the current state s_k and the emitted volume e_k, which represents the severity of the braking event through dissipated energy and deceleration (Eq. (3)). Green regions correspond to state decreases associated with mild braking, while red regions indicate state increases triggered by sufficiently severe braking events. The contour lines quantify the magnitude of Δs_k. The amplitude of the state increase does not depend on a single braking parameter, but on the interaction between the current surface state s_k and the severity of the event as expressed by e_k. Only sufficiently energetic events (red zone) trigger increases in s_k, whereas milder events (green zone) promote its decrease. Note that the smaller s_k is, the easier it is to fall in the red zone, returning to a higher s_k. (For interpretation of the references to colour in this figure legend, the reader is referred to the Web version of this article.)

3.2. Baseline emissions

To study the baseline emissions (i.e., before the modulation by s_k), we extract the subnetwork that computes $\hat{e}_k = f(\Delta v_k^2, d_k)$ from the trained network (Fig. 9, *a*) and make a parametric plot of $\hat{e}_k$ in Fig. 12. Emissions are initially proportional to the dissipated energy, i.e., proportional to $v_0^2 - v_f^2$ (note the x-axis is labeled with the linear velocities). However, emissions eventually grow faster (probably due to the temperature increase that is a consequence of the dissipated energy). Furthermore, the larger the deceleration, the earlier emissions depart from linearity.

3.3. Model accuracy

3.3.1. Individual brake events

Table 4 summarizes the model quality and presents the following metrics. Row 5 shows the root mean square prediction error (RMSE). Row 6 displays the maximum emission. Row 7 lists the root mean square error normalized by the maximum emission, which is less than 10% in all cases. Row 8 provides the mean emission, which is notably smaller for the WLTP cycles (datasets 3-5). Row 9 reports the root mean square error normalized by the mean emission. These figures are significantly larger than the NRMSE in row 7 because the mean emissions are usually 10 to 30 times smaller than the peak emissions.

A commonly used statistical indicator is the coefficient of

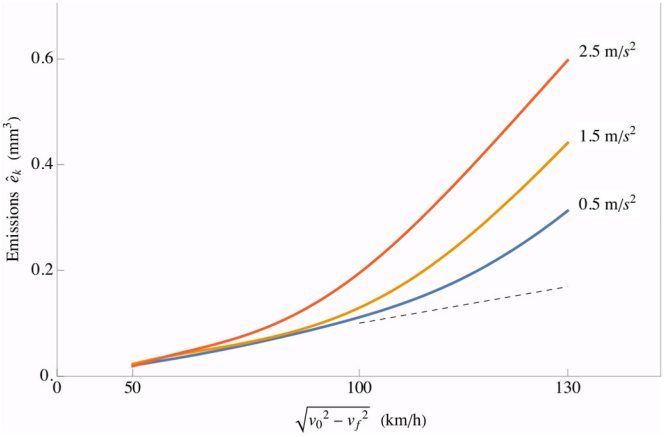

Fig. 12. Baseline emissions or, stationary component, as a function of dissipated energy and deceleration.

Table 4
Model quality indicators.

Dataset	1	2	3	4	5
	Randomized A (training set)	*Randomized B*	*WLTP 1-4 (four WLTP cycles)*	*WLTP 5 (after bedding with four WLTP cycles)*	*Mod. WLTP (seven cycles)*
Brake stops	*2772*	*1963*	*1212*	*303*	*2121*
Individual event emissions					
RMSE (mm^3)	*0.039*	*0.044*	*0.040*	*0.031*	*0.025*
Max emission (mm^3)	*0.763*	*0.548*	*0.802*	*0.589*	*0.657*
NRMSE	***5.1%***	***8.1%***	***5.0%***	***5.3%***	***3.9%***
Mean emission (mm^3)	*0.051*	*0.061*	*0.024*	*0.017*	*0.013*
NRMSE by Mean emissions	*76.4%*	*72.4%*	*169.7%*	*183.5%*	*194.0%*
R^2	***0.58***	***0.58***	***0.55***	***0.59***	***0.54***
Cumulative emissions					
Accumulated error	***−0.39%***	***−6.9%***	***−8.6%***	***−6.2%***	***−4.5%***
R^2on cumulative emissions	***99.9%***	***98.9%***	***99.2%***	***96.2%***	***99.5%***

determination (R^2), which is listed in row 10. R^2 represents the fraction of variance that the model describes. The remainder is noise caused by unmodelled features and measurement noise. Among the features that were not modeled are the mean velocity and the initial temperature (section 2.4.3). Among the measurement noise, there is the overlap between subsequent brake stops (i.e., particles emitted after one brake event may reach the measurement device with some delay and dispersion, overlapping the tail of the previous brake, as discussed in Fig. 7). In all cases, R^2 is about 0.54-0.59, which means the model predicts about 54-59% of the process variance. The rest, 41-46%, is unmodeled or noise (especially the overlap noise).

Fig. 14 compares the predicted and measured emissions in the first 250 cycles of the five datasets.

An autoregressive analysis of the fitting residuals shows weak autocorrelation that can be approximated by an AR (2) model, suggesting delayed emission, transport, and measurement effects extending up to two braking events, with a dominant one-step delay.

3.3.2. *Cumulative emissions*

The above considerations apply to predicting the emissions of a single brake stop. However, the main focus of this model is predicting the total emissions for a batch of brake events, such as a WLTP cycle. In this case, the noise that affects individual predictions tends to cancel out when looking at a batch of events (particularly the overlap noise). Due to delayed emission effects with a memory of up to two braking events, prediction accuracy for single events is reduced, while aggregation over multiple events progressively suppresses this effect; accordingly, binning events in groups of two or three results in increasing R^2 values for cumulative emissions. Fig. 13 compares the accumulated emissions to the predicted values across the five datasets. Dataset 1, which was used for training, is fitted almost perfectly. The remaining datasets have errors ranging from 4.5% to 8.6%. Evaluating R^2 we obtain the figures in the last row.

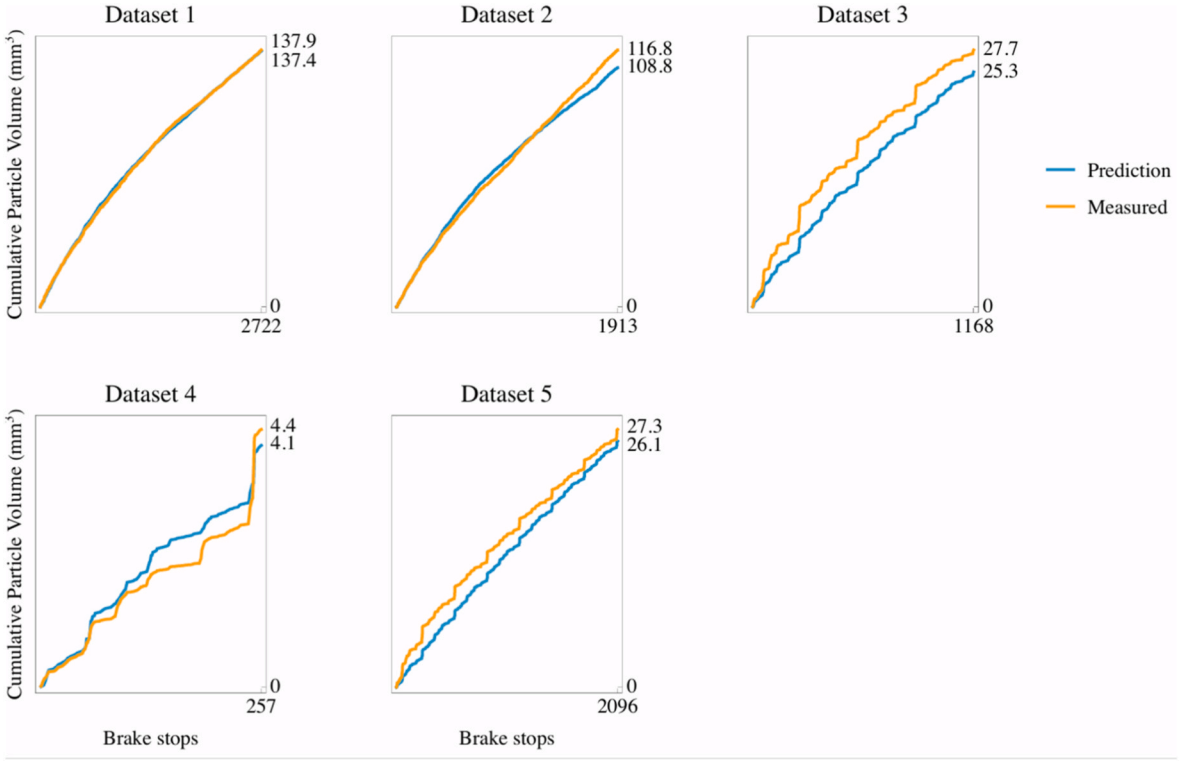

Fig. 13. Comparison of the accumulated emissions to the predicted values across the five datasets.

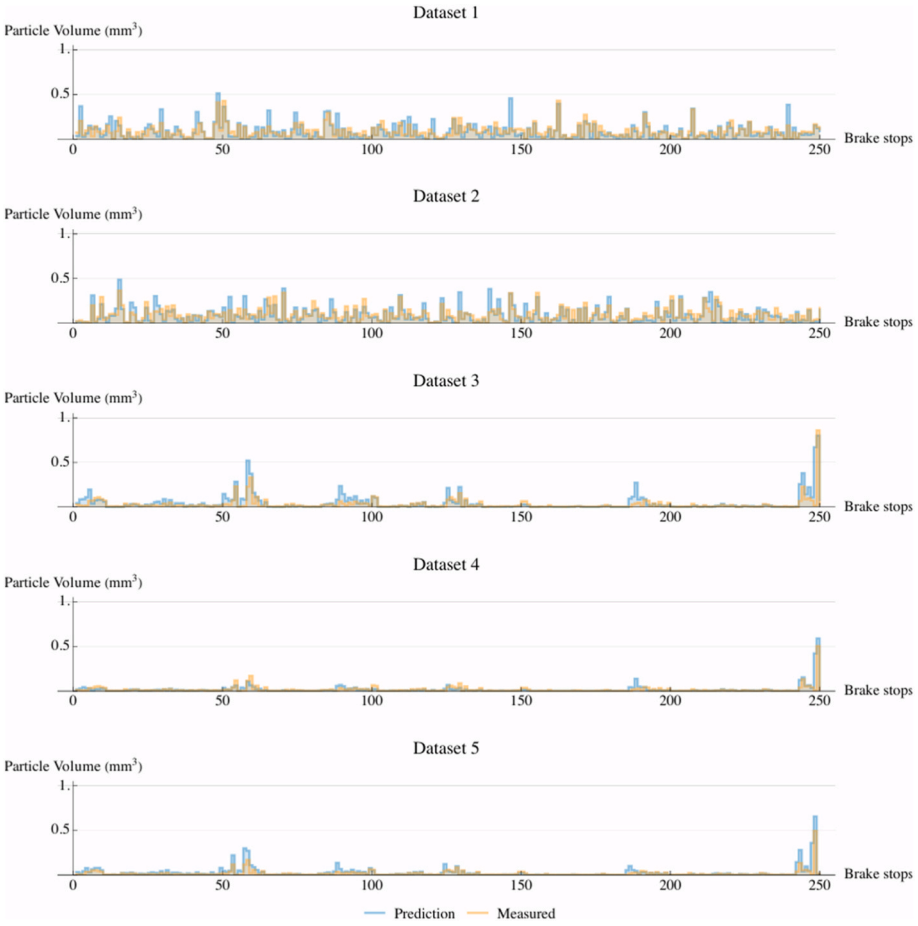

Fig. 14. Predicted and measured emissions in the first 250 cycles of the five datasets.

4. Discussion

This work introduces a recurrent neural network model designed to predict non-stationary brake emissions. The model was trained using experimental data collected from a reduced-scale dynamometer, where emissions were measured using an OPS.

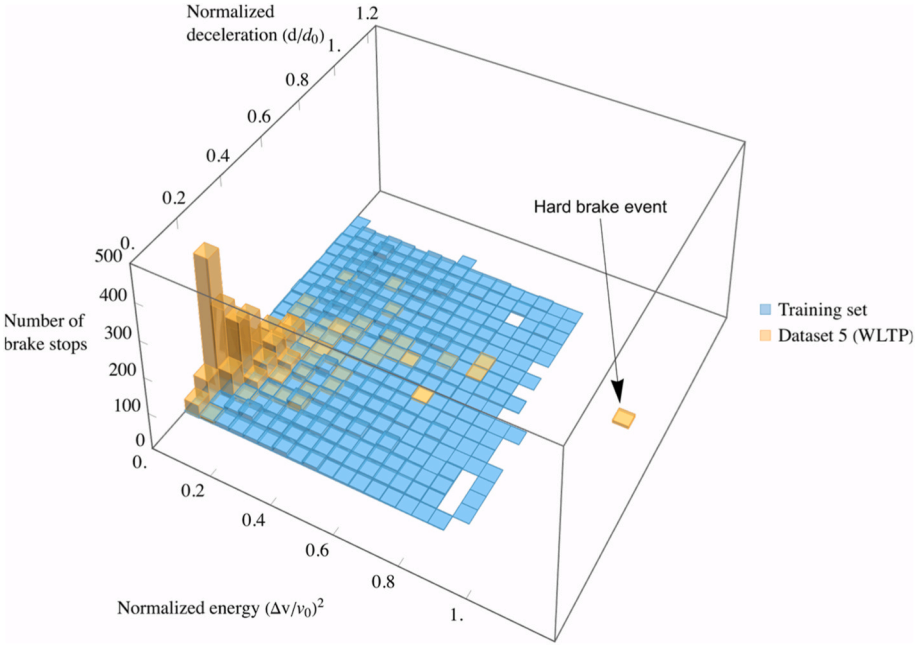

Fig. 15. Distribution of normalized dissipated energy and brake deceleration for the training set (Randomized A) and WLTP brake cycle.

4.1. Sampling and coverage of the parameter space

A novel aspect of the applied approach is the use of randomized tests involving variations in speed, mean speed, and brake deceleration. The domain is illustrated in Fig. 4, where points are uniformly spread within the trapezoidal area. Random pairs of values were combined with random brake deceleration values. Instead of controlling the initial brake temperature, the initial disc temperature was monitored and kept between 100 and 160 °C. It is also noteworthy that even if the transition temperature [47] were reached (10 % of the peak temperatures were above 200 °C), it is not expected to significantly affect the measured emitted particle volume under the investigated conditions, as the instrument detects particles as small as 0.3 μm, and any potential agglomerates would have a minimal impact on the emitted volume for the considered braking conditions.

The dataset in this study comprised five sets: two randomized tests, one WLTP cycle with fresh samples, one WLTP cycle with bedded pads, and a modified WLTP cycle with a minimum brake interval of 40 s.

Fig. 15 shows the coverage of the parameter space. The training dataset (Dataset 1) spans the entire range of input parameters. The WLTP datasets are fully within this range, although they mainly focus on low-energy brake events. However, there is one point outside the training distribution ("Out of Distribution", OOD). It is marked as "Hard Brake Event"[3] and corresponds to the sharp increase shown in Fig. 10. When predicting this event, the neural model extrapolates beyond the training data. As a result, we can expect significant errors in this particular prediction. Excluding this point, the remaining brake stops are within the training space, which explains why the prediction accuracy in Table 4 is acceptable for WLTP datasets.

4.2. Justification of input and output model parameters

The neural model used dissipated energy and brake deceleration as input variables, with emitted volume as the output. An important point we aimed to demonstrate is that using just these two inputs, and considering the history, can achieve very high R^2 values when predicting cumulative emissions, even though the R^2 values for individual events are moderate, ranging from 0.54 to 0.59. This relates to random measurement errors that offset each other when emissions are summed into cumulative values. The input variables that were intentionally excluded from the model are average velocity and initial brake temperature. In contrast, the temperature rise during braking is implicitly accounted for as a derivative parameter, because it depends on dissipated energy, brake deceleration, and average velocity.

4.3. Dynamics and steady-state components

The model consists of two parts: a stationary component, which depends only on dissipated energy and brake deceleration, and a state component, modeled by a state variable s, which serves as a scaling factor capturing surface effect variations caused by long-term (bedding process) or short-term (changing braking parameters) memory effects. This approach is ideal for defining steady-state regimes because transition effects are solely incorporated in the state component. Consequently, the steady-state part remains independent of memory effects.

From Fig. 12, the trends of the stationary components are linear with dissipated energy up to an approximate brake stop, which begins around 70 km/h until the vehicle comes to a complete stop. Beyond this threshold, deceleration becomes more significant, and the relationship becomes nonlinear, with power increasing in proportion to brake deceleration. Cubic trends with velocity have already been observed [11,28,40] and are consistent with the relationship shown in Fig. 12. However, measurements were often affected by high noise, and the relationship with deceleration does not always correlate with increasing emissions, as history effects may mask its true role, resulting in contrasting findings in the literature [11,30]. The mean velocity and initial brake temperature were intentionally excluded as input variables from the model. Including initial temperature and mean velocity could improve the model's R^2, but requires more training/test data, and will be explored in future studies. Conversely, the temperature rise during braking is treated as a derived parameter because it correlates with dissipated energy, brake deceleration, and average velocity.

As mentioned, the recurrent component, s, can be interpreted as the influence of the surface state on the emissions, which depends on the previous brakes. For example, a high-intensity braking event can cause a quick rise in the system state and subsequent emissions. These effects may last and continue to affect later brake stops.

The influence of previous braking events on the system state causes fluctuations, making it hard to identify consistent and monotonic trends in the bedding process with standard models. This is especially true for brake deceleration, as its effect becomes significant only above a certain energy threshold. Notably, the recurrent component was able to capture both short-term effects, such as those induced by varying braking parameters, and long-term effects, such as the bedding process.

The recurrent component, s, represents an internal state inferred from the emission dynamics and is introduced to account for history-dependent effects observed in the experimental data. Its evolution exhibits systematic trends: sequences of mild braking are associated with a gradual decrease in s, whereas sufficiently severe braking events produce temporary increases, as described by the dependence of Δs_k on the emitted volume e_k (Fig. 11). Since e_k embeds the combined effects of dissipated energy and brake deceleration (Eq. (3)), variations in s reflect the influence of preceding braking events as captured by the model formulation. The state, s, is therefore treated as a phenomenological quantity or macroscopic descriptor of surface history derived from the fitted dynamics, without assigning it to specific microscopic surface mechanisms, as it could not be directly linked to specific surface topographies.

4.4. Tribological perspective

The following discussion is intended to provide a tribological interpretation of the observed behaviors, rather than a correlation between surface topographies and variations in internal state, s, as detailed surface-topography characterization was beyond the scope of this study.

The overall wear regime observed in the applied tests can be classified as mild sliding conditions, as the sliding temperatures remained below the critical threshold of 250–400 °C, typically associated with severe wear and binder degradation in resin-based friction materials [59,60].

The observed progressive decrease in emissions is consistent with bedding stabilization trends reported for brake materials. It is acknowledged that during the bedding process, the mating surfaces develop friction layers, and the pad surface progressively increases its coverage factor within the friction layer, which is characterized by the high compaction of mechanically mixed iron oxides and pad constituents. Meanwhile, the disc undergoes significant asperity removal and plastic deformation, eventually forming thin transfer layers [24,25,46]. As a result of these processes, the formation of friction layers contributes to overall improved wear resistance and reduced emissions, ultimately leading to steady-state, or pseudo-steady-state conditions, depending on the testing parameters and the model considered. Asymptotic limits are conceptually accepted within the framework of the third body theory [61] when the ejection and deposition rates at the surface converge toward steady values. Such behavior has been observed in dynamometer studies under repeated braking conditions [25], and more generally in pin-on-disc experiments.

Regarding the component of the state, s, that captures fluctuations in

[3] This brake stops corresponds to the following parameters: $v_0 = 132.4$ km/h, $v_f = 33.9$ km/h, $d = 1.805$ m/s^2.

emissions induced by the brake history, meaningful interpretation can be drawn from studies that conducted a posteriori surface analysis. The studies [11,62] have compared pad surfaces after harsh and mild braking conditions. Following harsh braking, the surfaces exhibit a lower coverage of the friction layer, suggesting that the combination of high speed and elevated temperature increases the overall wear rate, inhibiting the formation of compacted patches and facilitating the release of particles from the tribological system. A similar effect of temperature on particle emissions was also observed in mesoscale surface simulations [63]. On the other hand, a decrease in the state, *s*, during light braking can be associated with the combination of low wear rate and compaction processes of the wear products, which promote the stabilization and compaction of the friction layer, reducing the particle release. The described mechanisms can be generally interpreted within the framework of the third body theory, and their influence on brake materials is often referred to as *reservoir dynamics* [64]. Highly challenging in situ observation of surface evolution has been reported by Ref. [64,65]. However, in most studies, interpretations on the surface evolution are derived from the emission signals [10,11] or a posteriori surface analysis [11,45,46].

In this work, we introduced the concept of internal state to predict emissions as particle volume in the size range of 0.3 to 10 μm, without relying on a direct correlation with the surface topographies. For this, we emphasized that the recurrent state introduced here should be regarded as a macroscopic phenomenological descriptor derived from emission dynamics, rather than as a direct indicator of specific surface topographies, material degradation, or potential brake system evolution.

Future research should focus on mechanical and surface characterization to explicitly formulate the variability of these concepts, for which the present study provides the conceptual foundation.

5. Conclusions

The methodology developed in this work introduces a novel definition of steady states and the concept of emissions-related states using a recurrent state.

Additionally, this work utilizes a structured neural modeling tool to analyze key characteristics of brake emissions. The modules of the neural model are interpretable and can be extracted, facilitating a more accurate interpretation and visualization of the phenomenon.

Notably, the model accurately predicts cumulative brake emissions with a high coefficient of determination using only dissipated energy and brake deceleration as inputs. Initial temperature and average velocity were intentionally considered as unmodeled noise.

Future research should focus on applying this approach to real-world vehicle applications (for example, developing ecological driving that minimizes emissions, especially for electric vehicles). Addressing sources of uncertainty, such as sample variability, measurement errors, or sensitivity to initial conditions, will require further experimental validation through controlled brake emission tests and repeated measurements. Exploring other metrics, such as particle number and distribution, will also be important to enhance the model's applicability and robustness.

Finally, examining the surface conditions during bedding and transient fluctuations and their correlation with the state, *s*, will strengthen the physical interpretation of the model.

CRediT authorship contribution statement

Stefano Candeo: Writing – original draft, Visualization, Validation, Software, Methodology, Investigation, Formal analysis, Data curation, Conceptualization. **Ana Paula Nogueira:** Resources, Project administration. **Giovanni Straffelini:** Writing – review & editing, Validation, Supervision, Project administration, Conceptualization. **Mauro Da Lio:** Writing – review & editing, Writing – original draft, Visualization, Validation, Supervision, Software, Project administration, Methodology, Investigation, Formal analysis, Data curation, Conceptualization.

Declaration of generative AI and AI-assisted technologies in the writing process

During the preparation of this work, the author Stefano Candeo used ChatGPT and Copilot for text revision purposes, including spelling, grammar, and style adjustments. After using this tool, the authors reviewed and edited the content as needed and took full responsibility for the content of the publication.

Declaration of competing interest

The authors declare that they have no known competing financial interests or personal relationships that could have appeared to influence the work reported in this paper.

Data availability

The data that has been used is confidential.

References

[1] T. Grigoratos, G. Martini, Non-exhaust traffic related emissions - brake and tyre wear PM, JRC Publication. Reposit. (2016), https://doi.org/10.2790/2200.
[2] R.M. Harrison, A.M. Jones, J. Gietl, J. Yin, Estimation of the contributions of brake dust, tire wear, and resuspension to non-exhaust traffic particles derived from atmospheric measurements, Environ. Sci. Technol. 46 (3) (2012) 6523–6530, https://doi.org/10.1021/es300894r.
[3] N. Bukowiecki, C.N. Zwicky, M. Gehrig, A. Lienemann, M. Furger, A.H. Hauri, C. Hueglin, U. Baltensperger, Real-world emission factors for antimony and other brake wear related trace elements: size-segregated values for light and heavy duty vehicles, Environ. Sci. Technol. 43 (21) (2009) 8072–8078, https://doi.org/10.1021/es9006096.
[4] M. Gasser, M. Riediker, L. Mueller, P.P. Perrenoud, F. Blank, P. Gehr, B. Rothen-Rutishauser, Toxic effects of brake wear particles on epithelial lung cells in vitro, Part. Fibre Toxicol. 6 (1) (2009) 30, https://doi.org/10.1186/1743-8977-6-30.
[5] S. Lawrence, R. Sokhi, K. Ravindra, H. Mao, H.D. Prain, I.D. Bull, Source apportionment of traffic emissions of particulate matter using tunnel measurements, Atmos. Environ. 77 (2013) 548–557, https://doi.org/10.1016/j.atmosenv.2013.03.040.
[6] T. Grigoratos, G. Martini, Brake wear particle emissions: a review, Environ. Sci. Pollut. Res. 22 (4) (2015) 2491–2504, https://doi.org/10.1007/s11356-014-3696-8.
[7] B.D. Garg, S.H. Cadle, P.A. Mulawa, P.J. Groblicki, C. Laroo, G.A. Parr, Brake wear particulate matter emissions, Environ. Sci. Technol. 34 (21) (2000) 4463–4469, https://doi.org/10.1021/es001108h.
[8] P.G. Sanders, N. Xu, T.M. Dalka, M.M. Maricq, Airborne brake wear debris: size distributions, composition, and a comparison of dynamometer and vehicle tests, Environ. Sci. Technol. 37 (18) (2003) 4060–4069, https://doi.org/10.1021/es034145s.
[9] B. Giechaskiel, T. Grigoratos, P. Dilara, T. Karageorgiou, L. Ntziachristos, Z. Samaras, Light-duty vehicle brake emission factors, Atmosphere 15 (1) (2024) 97, https://doi.org/10.3390/atmos15010097.
[10] S. Gramstat, T. Mertens, R. Waninger, D. Lugovyy, Impacts on brake particle emission testing, Atmosphere 11 (10) (2020) 1132, https://doi.org/10.3390/atmos11101132.
[11] S. Candeo, M. Leonardi, S. Gialanella, S. Straffelini, Influence of contact pressure and velocity on the brake behaviour and particulate matter emissions, Wear (2023) 514–515, https://doi.org/10.1016/j.wear.2022.204579, 204579.
[12] S. Candeo, A.P. Nogueira, S. Gialanella, S. Straffelini, Wear-emission correlation in brake materials, Wear (2025) 562–563, https://doi.org/10.1016/j.wear.2024.205650, 205650.
[13] L. Storch, A. Mayer, T. Lutz, C. Wüthrich, M. Schönenberger, T. Nussbaumer, Comprehensive analysis of current primary measures to mitigate brake wear particle emissions from light-duty vehicles, Atmosphere 14 (4) (2023) 712, https://doi.org/10.3390/atmos14040712.
[14] A. Sinha, S. Candeo, G. Straffelini, S. Gialanella, TEM characterization of particulate matter emissions from the bedding stage of a Cu-free brake friction material, Tribol. Int. 188 (2023) 108832, https://doi.org/10.1016/j.triboint.2023.108832.
[15] A. Sinha, G. Ischia, C. Menapace, S. Gialanella, Experimental characterization protocols for wear products from disc brake materials, Atmosphere 11 (10) (2020) 1102, https://doi.org/10.3390/atmos11101102.
[16] S.H. Woo, H. Jang, M.Y. Na, H.J. Chang, S. Lee, Characterization of brake particles emitted from non-asbestos organic and low-metallic brake pads under normal and harsh braking conditions, Atmos. Environ. 278 (2022) 119089, https://doi.org/10.1016/j.atmosenv.2022.119089.

[17] C. Neukirchen, A. Mayer, L. Storch, T. Lutz, C. Wüthrich, T. Nussbaumer, Comprehensive elemental and physical characterization of vehicle brake wear emissions from two different brake pads following the global technical regulation methodology, J. Hazard Mater. 482 (2025) 136609, https://doi.org/10.1016/j.jhazmat.2024.136609.
[18] J. Kukutschová, V. Moravec, P. Tomášek, J. Matějka, K. Smolík, V. Schwarz, Z. Seidler, V. Šafář, On airborne nano/micro-sized wear particles released from low-metallic automotive brakes, Environ. Pollut. 159 (4) (2011) 998–1006, https://doi.org/10.1016/j.envpol.2010.11.036.
[19] H. Niemann, H. Winner, C. Asbach, H. Kaminski, G. Frentz, R. Milczarek, Influence of disc temperature on ultrafine, fine, and coarse particle emissions of passenger car disc brakes with organic and inorganic pad binder materials, Atmosphere 11 (10) (2020) 1060, https://doi.org/10.3390/atmos11101060.
[20] T. Grigoratos, M. Giorgio, S. Heinz, Analysis of WLTP typical driving conditions that affect non-exhaust particle emissions, JRC Tech. Rep. (2016), https://doi.org/10.2790/283623.
[21] T. Grigoratos, M. Mathissen, R. Vedula, A. Mamakos, C. Agudelo, S. Gramstat, B. Giechaskiel, Statistical assessment and temperature study from the interlaboratory application of the WLTP–brake cycle, Atmosphere 11 (12) (2020) 1309, https://doi.org/10.3390/atmos11121309.
[22] T. Grigoratos, M. Mathissen, R. Vedula, A. Mamakos, C. Agudelo, S. Gramstat, B. Giechaskiel, Interlaboratory study on brake particle emissions—Part I: particulate matter mass emissions, Atmosphere 14 (3) (2023) 498, https://doi.org/10.3390/atmos14030498.
[23] R. Vedula, C. Agudelo, J. Grochowicz, B. Giechaskiel, Interlaboratory study on brake particle emissions—Part II: particle number emissions, Atmosphere 14 (3) (2023) 424, https://doi.org/10.3390/atmos14030424.
[24] V. Matějka, I. Metinöz, J. Wahlström, M. Alemani, G. Perricone, On the running-in of brake pads and discs for dyno bench tests, Tribol. Int. 115 (2017) 424–431, https://doi.org/10.1016/j.triboint.2017.06.008.
[25] S. Candeo, A.P. Nogueira, M. Leonardi, G. Straffelini, A study of friction, wear and particulate emissions during the bedding stage of a Cu-free friction material, Wear (2021) 486–487, https://doi.org/10.1016/j.wear.2021.204095, 204095.
[26] D. Hesse, C. Hamatschek, K. Augsburg, T. Weigelt, A. Prahst, S. Gramstat, Testing of alternative disc brakes and friction materials regarding brake wear particle emissions and temperature behavior, Atmosphere 12 (4) (2021) 436, https://doi.org/10.3390/atmos12040436.
[27] S. Trepte, Einlaufverhalten technischer Reibbeläge, ATZ Automobiltechnische Zeitschrift 103 (12) (2001) 1168–1177.
[28] H. Niemann, H. Winner, C. Asbach, H. Kaminski, M. Zessinger, M. Brandau, Map based simulation of brake wear particle emissions. EuroBrake 2020 Conference Proceedings, 2020, https://doi.org/10.46720/EB2020-STP-022.
[29] S. Candeo, F. Varriale, A.P. Nogueira, S. Gialanella, G. Straffelini, Performance of a cast-iron and WC Co-free iron-based coated disc under mild and severe brake conditions, Wear (2024) 548–549, https://doi.org/10.1016/j.wear.2024.205369, 205369.
[30] S. Vasiljević, J. Glišović, J. Lukić, D. Miloradović, M. Stanojević, M. Đorđević, Analysis of parameters influencing the formation of particles during the braking process: experimental approach, Atmosphere 14 (11) (2023), https://doi.org/10.3390/atmos14111618.
[31] H. Hagino, A. Iwata, T. Okuda, Iron oxide and hydroxide speciation in emissions of brake wear particles from different friction materials using an X-ray absorption fine structure, Atmosphere 15 (1) (2024) 49, https://doi.org/10.3390/atmos15010049.
[32] G. Perricone, et al., A Concept for Reducing PM10 Emissions for Car Brakes by 50%. Wear vols. 396–397, 2018, pp. 135–145, https://doi.org/10.1016/j.wear.2017.06.018.
[33] C. Hamatschek, et al., Comparative study on the friction behaviour and the particle formation process between a laser cladded brake disc and a conventional grey cast iron disc, Metals 13 (2) (2023) 300, https://doi.org/10.3390/met13020300.
[34] C. Hamatschek, D. Hesse, K. Augsburg, S.G.A. Straffelini, Comparison of the Particle Emission Behaviour of Automotive Drum and Disc Brakes, Springer Nature, 2021.
[35] M. Hascoët, L. Adamczak, At source brake dust collection system, Results Eng. 5 (2020) 100083, https://doi.org/10.1016/j.rineng.2019.100083.
[36] S. Gramstat, M. Hascoet, C. Rocca-Serra, L. Adamczak, Potentials and challenges of a brake particle emission collecting system, SAE Tech. Paper (2020), https://doi.org/10.4271/2020-01-1635.
[37] I.S. Hwang, Y.L. Lee, A study on the pressure drop characteristics of a passive filter system for collecting fine brake dust, Int. J. Automot. Technol. 22 (2021), https://doi.org/10.1007/s12239-021-0110-7.
[38] F. Keller, T. Wörz, A. Beck, M. Kopriva, M. Uhlir, S. Pfannkuch, Development of an active brake dust particle filter system to reduce brake dust emissions, EB2023-EFA-007, EuroBrake Proceedings (2023).
[39] I.S. Hwang, J.T. Park, Y.L. Lee, Feasibility of a porous ceramic filter for collecting brake fine dust, Int. J. Automot. Technol. 23 (2022), https://doi.org/10.1007/s12239-022-0048-4.
[40] H. Hagino, M. Oyama, S. Sasaki, Airborne brake wear particle emission due to braking and accelerating, Wear 334–335 (2015) 44–48, https://doi.org/10.1016/j.wear.2015.04.012.
[41] Z. Men, et al., Determining factors and parameterization of brake wear particle emission, J. Hazard Mater. 434 (2022) 128856, https://doi.org/10.1016/j.jhazmat.2022.128856.
[42] S.H. Woo, Y. Kim, S. Lee, Y. Choi, S. Lee, Characteristics of brake wear particle emissions under various test driving cycles, Wear 480–481 (2021) 203936, https://doi.org/10.1016/j.wear.2021.203936.
[43] W. Songkitti, S. Sa-Ard-iam, C. Plengsa-Ard, E. Wirojaskunchai, Effects of payloads on non-exhaust PM emissions from a hybrid electric vehicle during a braking sequence, Aerosol Air Qual. Res. 22 (7) (2022), https://doi.org/10.4209/aaqr.220150.
[44] Y. Liu, et al., Brake wear induced PM10 emissions during the world harmonised light-duty vehicle test procedure-brake cycle, J. Clean. Prod. 361 (2022) 132278, https://doi.org/10.1016/j.jclepro.2022.132278.
[45] J. Park, et al., Analysis of wear induced particle emissions from brake pads during the worldwide harmonized light vehicles test procedure (WLTP), Wear (2021) 466–467, https://doi.org/10.1016/j.wear.2020.203539, 203539.
[46] M. Thévenot, J.F. Brunel, F. Brunel, M. Briatte, Y. Desplanques, P. Dufrénoy, Identification of particle emission mechanisms during dry friction with thermomechanical operando monitoring, Wear 570 (2025) 205974, https://doi.org/10.1016/j.wear.2025.205974.
[47] O. Nosko, U. Olofsson, Quantification of ultrafine airborne particulate matter generated by the wear of car brake materials, Wear 374–375 (2017) 92–96, https://doi.org/10.1016/j.wear.2017.01.003.
[48] M. Alemani, O. Nosko, I. Metinoz, U. Olofsson, A study on emission of airborne wear particles from car brake friction pairs, SAE Int. J. Mater. Manuf. 9 (1) (2016) 147–157, https://doi.org/10.4271/2015-01-2665.
[49] K.M. Jensen, I.F. Santos, Estimation of passenger car brake pad temperatures and wear from on-road data and lumped multi-physical models, Wear 578–579 (2025) 206138, https://doi.org/10.1016/j.wear.2025.206138.
[50] N. Wei, et al., Applying machine learning to construct braking emission model for real-world road driving, Environ. Int. 166 (2022) 107386, https://doi.org/10.1016/j.envint.2022.107386.
[51] Y. Liu, et al., PM10 prediction for brake wear of passenger car during different test driving cycles, Chemosphere 305 (2022) 135481, https://doi.org/10.1016/j.chemosphere.2022.135481.
[52] V. Ricciardi, M. Schiele, D. Hesse, P. Hauschild, K. Augsburg, Artificial neural network regression models for the prediction of brake-related emissions. EuroBrake 2020 Conference Proceedings, 2020, https://doi.org/10.46720/EB2020-STP-050.
[53] M. Rahimi, S. Candeo, M. Da Lio, F. Biral, J. Wahlström, D. Bortoluzzi, A novel approach for brake emission estimation based on traffic microsimulation, vehicle system dynamics, and machine learning modeling, Atmos. Pollut. Res. 14 (10) (2023) 101872, https://doi.org/10.1016/j.apr.2023.101872.
[54] S. Candeo, M. Federici, M. Leonardi, G. Straffelini, Brake performance maps for a Cu-free friction material with different scorching conditions, Tribol. Trans. 64 (3) (2021) 540–550, https://doi.org/10.1080/10402004.2020.1869360.
[55] M. Mathissen, et al., A novel real-world braking cycle for studying brake wear particle emissions, Wear 414–415 (2018) 219–226, https://doi.org/10.1016/j.wear.2018.07.020.
[56] O. Nosko, U. Olofsson, Effective density of airborne wear particles from car brake materials, J. Aerosol Sci. 107 (2017) 94–106, https://doi.org/10.1016/j.jaerosci.2017.02.014.
[57] M. Da Lio, M. Piccinini, F. Biral, Robust and sample-efficient estimation of vehicle lateral velocity using neural networks with explainable structure informed by kinematic principles, IEEE Trans. Intell. Transport. Syst. 24 (12) (2023) 13670–13684, https://doi.org/10.1109/TITS.2023.3303776.
[58] A. Cherubini, G.P.R. Papini, A. Plebe, M. Piazza, M. Da Lio, Bootstrapped neural models for predicting self-driving vehicle collisions with quantified confidence: offline and online applications, IEEE Trans. Intell. Veh. (2024) 1–21, https://doi.org/10.1109/TIV.2024.3512786.
[59] A.L. Cristol-Bulthé, Y. Desplanques, G. Degallaix, Y. Berthier, Mechanical and chemical investigation of the temperature influence on the tribological mechanisms occurring in OMC/cast iron friction contact, Wear 264 (9–10) (2008) 815–825, https://doi.org/10.1016/j.wear.2006.12.080.
[60] K. Tanaka, S. Ueda, N. Noguchi, Fundamental studies on the brake friction of resin-based friction materials, Wear 23 (3) (1973) 349–365, https://doi.org/10.1016/0043-1648(73)90022-7.
[61] N. Fillot, I. Iordanoff, Y. Berthier, Wear modeling and the third body concept, Wear 262 (7–8) (2007) 949–957, https://doi.org/10.1016/j.wear.2006.10.011.
[62] J.W. Kim, B.S. Joo, H. Jang, The effect of contact area on velocity weakening of the friction coefficient and friction instability: a case study on brake friction materials, Tribol. Int. 135 (2019) 38–45, https://doi.org/10.1016/j.triboint.2019.02.034.
[63] J. Wahlström, Towards a cellular automaton to simulate friction, wear, and particle emission of disc brakes, Wear 313 (1–2) (2014) 75–82, https://doi.org/10.1016/j.wear.2014.02.014.
[64] S. Gramstat, Methoden der in-situ Visualisierung der Reibzonendynamik trockenlaufender Reibpaarungen unter Ergänzung physikalischer und chemischer Charakterisierungen der Reibpartner, Dissertation, 2014.
[65] M. Eriksson, J. Lord, S. Jacobson, Wear and contact conditions of brake pads: dynamical in situ studies of pad on glass, Wear 249 (2001) 272–278.